

Quantifying the impact of the surface roughness of ice crystals on the backscattering properties for lidar-based remote sensing applications

Masanori Saito¹, Ping Yang¹, Lei Bi², Jens Reichardt³, Bastiaan Van Diedenhoven⁴, Kaori Sato⁵, and Zhien Wang⁶

¹Texas A&M University

²Zhejiang University

³Deutscher Wetterdienst

⁴Columbia University / NASA Goddard Institute for Space Studies

⁵Research Institute for Applied Mechanics, Kyushu University

⁶University of Colorado Boulder

December 10, 2022

Abstract

Impacts of small-scale surface irregularities, or surface roughness, of atmospheric ice crystals on lidar backscattering properties are quantified. Geometric ice crystal models with various degrees of surface roughness and state-of-the-science light-scattering computational capabilities are used to simulate single-scattering properties across the entire practical size parameter range. The simulated bulk lidar and depolarization ratios of polydisperse ice crystals at 532 nm are strongly sensitive to the degree of surface roughness. Comparisons of these quantities between the theoretical simulations and counterparts inferred from spaceborne lidar observations for cold cirrus clouds suggest a typical surface roughness range of 0.03–0.15, which is most consistent with direct measurements of scanning electron microscopic images. The degree of surface roughness needs to be accounted for to properly interpret lidar backscattering observations of ice clouds.

Hosted file

951454_0_art_file_10519905_rmlbd5.docx available at <https://authorea.com/users/533452/articles/612258-quantifying-the-impact-of-the-surface-roughness-of-ice-crystals-on-the-backscattering-properties-for-lidar-based-remote-sensing-applications>

1 **Quantifying the impact of the surface roughness of ice crystals on the backscattering**
2 **properties for lidar-based remote sensing applications**

3 **Masanori Saito^{1,*} and Ping Yang¹**

4 ¹Department of Atmospheric Sciences, Texas A&M University, College Station, TX, USA.

5

6 Corresponding author: Masanori Saito (masa.saito@tamu.edu)

7 **Key Points:**

- 8 • Sensitivities of the backscattering properties to the surface roughness of atmospheric ice
9 crystals are theoretically investigated.
- 10 • The depolarization ratio is markedly sensitive to the degree of surface roughness of ice
11 crystals.
- 12 • The lidar and depolarization ratios observed by CALIOP are well explained with the ice
13 model with degree of surface roughness 0.03–0.15.

14 **Abstract**

15 Impacts of small-scale surface irregularities, or surface roughness, of atmospheric ice crystals on
16 lidar backscattering properties are quantified. Geometric ice crystal models with various degrees
17 of surface roughness and state-of-the-science light-scattering computational capabilities are used
18 to simulate single-scattering properties across the entire practical size parameter range. The
19 simulated bulk lidar and depolarization ratios of polydisperse ice crystals at 532 nm are strongly
20 sensitive to the degree of surface roughness. Comparisons of these quantities between the
21 theoretical simulations and counterparts inferred from spaceborne lidar observations for cold
22 cirrus clouds suggest a typical surface roughness range of 0.03–0.15, which is most consistent
23 with direct measurements of scanning electron microscopic images. The degree of surface
24 roughness needs to be accounted for to properly interpret lidar backscattering observations of ice
25 clouds.

26

27 **Plain Language Summary**

28 Lidar (Light Detection and Ranging) instruments on satellites use reflected, or backscattered,
29 laser beams to investigate ice clouds in the atmosphere. However, it has long been a challenge to
30 interpret lidar signals, called backscattering properties, to accurately infer ice cloud
31 characteristics. This study uses theoretical simulations to investigate how small-scale surface
32 irregularities of ice crystals affect the lidar signals reflected from ice clouds. These simulations
33 demonstrate the significant impacts of the small-scale surface irregularities of ice crystals on
34 backscattering. Comparisons between the theoretical simulations and satellite lidar observations
35 confirm the necessity to assume a moderate degree of small-scale surface irregularities to explain
36 lidar observations of typical ice clouds.

37 **1 Introduction**

38 Atmospheric ice crystals often exhibit small-scale surface irregularities or roughness
39 (Cross, 1968; Magee et al., 2014), which are caused mainly by depositional growth and
40 sublimation under super- and sub-saturated conditions. Roughening of ice crystal surfaces has
41 been observed via laboratory experiments (Pfalzgraff et al., 2010; Schnaiter et al., 2016;
42 Butterfield et al., 2017) and in-situ measurements in cirrus clouds (Ulanowski et al., 2014;
43 Magee et al., 2021). Compared to pristine ice crystals with smooth surfaces, those with
44 roughened surfaces tend to have featureless phase function near backscattering angles, which
45 corresponds to smaller asymmetry factor values. It has been demonstrated that surface roughness
46 is a critical factor affecting passive remote sensing of ice cloud properties (Yang et al., 2008; van
47 Diedenhoven et al., 2013; Hioki et al., 2016) and estimation of ice cloud radiative effects (Yi et
48 al., 2013; Järvinen et al., 2018).

49 Surface roughness effects on the shortwave scattering properties of ice crystals have been
50 theoretically investigated based mainly on the principles of geometric optics (Macke et al., 1996;
51 Yang & Liou, 1998), because rigorous light-scattering computational methods lead to an
52 enormous computational burden for typical ice crystal sizes in the ultra-violet to near-infrared
53 spectral regime. However, geometric optics methods compute inaccurate single-scattering
54 properties of ice crystals near the backscattering angle due to inherent limitations, particularly a
55 lack of consideration of coherent backscattering enhancement (CBE). The more sophisticated
56 Physical Geometric Optics Method (PGOM), implemented by either the surface-integral or
57 volume-integral approach, fully considers phase interference of outgoing waves (Yang & Liou,
58 1996, 1997), and produces consistent numerical results (Yang et al., 2019). PGOM has been
59 numerically implemented for relatively simple ice particles (e.g., columns and plates) and

60 aggregates of convex particles (e.g., 8-column aggregates; see Yang et al., 2019 and references
61 cited therein).

62 The challenge in light-scattering computations for nonspherical particles, particularly in
63 the case of large size parameters, has long hampered the accuracy of inferred ice cloud properties
64 from lidar observations. Specifically, the physical interpretation of the backscattering properties
65 of ice crystals, such as the lidar and depolarization ratios, is largely empirical (Zhou & Yang,
66 2015; Ding et al., 2016), leading to substantial uncertainties in inferred ice cloud quantities. As
67 surface roughening in ice crystals is prevalent globally in ice clouds (van Diedenhoven et al.,
68 2020), this study aims to quantify the impact of surface roughness based on a combination of
69 state-of-the-science rigorous and approximate light-scattering computational algorithms applied
70 to geometrically roughened ice crystal models.

71

72 **2 Methods**

73 2.1 Geometrically roughened ice crystal models

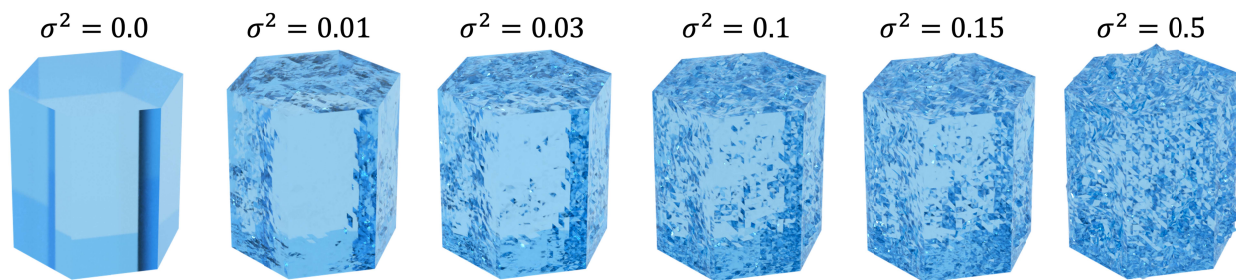
74 In this study, the degree of surface roughness is defined in terms of the variance (σ^2) of
75 the two-dimensional Gaussian distribution $P(Z_x, Z_y)$ of local planar surface slopes (Liu et al.,
76 2013; Saito & Yang, 2022a), which originates from a rough ocean surface model (Cox & Munk,
77 1954) and is described as

$$78 \quad P(Z_x, Z_y) = \frac{1}{\pi\sigma^2} e^{-[(Z_x^2 + Z_y^2)/\sigma^2]}, \quad (1)$$

79 where $Z_x = \partial Z / \partial x$ and $Z_y = \partial Z / \partial y$ are the slopes of local planar facets along two axes
80 orthogonal to the normal direction Z in reference to an un-tilted regular crystal facet described

81 below. The original facets of a regular hexagonal column are discretized into many small
82 triangular facets with a maximum facet length of approximately 1/40 of those original facets.
83 These small facets are tilted according to the probability density of the surface slope defined by a
84 2D Gaussian distribution with the specified σ^2 . Technical details on geometrically roughened ice
85 crystal models are discussed in Liu et al. (2013). In this study, the macroscopic crystal shape is a
86 regular hexagonal column with an aspect ratio of unity. Note that Okamoto et al. (2020) have
87 investigated the backscattering properties of many other particle shapes without surface
88 roughness.

89 Figure 1 illustrates geometrically roughened hexagonal column models with various
90 degrees of surface roughness ranging from $\sigma^2 = 0$ (smooth) to 0.5 (severely roughened). A
91 crystal surface with a higher degree of surface roughness has more complex texture. Neshyba et
92 al. (2013) developed a stereographic method to estimate the surface roughness using scanning
93 electron microscopic (SEM) images of an ice crystal, and found that surface roughness is well
94 represented by a Weibull distribution with a shape parameter 0.7–0.95 (Butterfield et al., 2017).
95 The Weibull distribution with a shape parameter of unity is equivalent to the 2D Gaussian
96 distribution.



98 **Figure 1.** Illustration of geometric hexagonal column ice crystal models with degree of surface
99 roughness 0, 0.01, 0.03, 0.1, 0.15, and 0.5.

100

101 2.2 Computational methods

102 To simulate the single-scattering properties of roughened ice crystals, we use the
103 numerically accurate Invariant-Imbedding T-matrix Method (IITM; Johnson, 1988; Bi & Yang,
104 2014; and references cited therein), for the largest possible size parameter cases. As the
105 computational burden increases exponentially with the size parameter, previous studies limited
106 simulations of geometrically roughened ice crystals to size parameter kD up to ~ 150 , where the
107 modified wavenumber is $k = 2\pi/\lambda$, D is the particle maximum dimension, and λ is the
108 wavelength. Leveraging the computational capabilities provided by the Texas A&M University
109 High-Performance Research Computing (TAMU HPRC) facilities, we perform scattering
110 property simulations with IITM for roughened ice crystals with kD up to approximately 316.

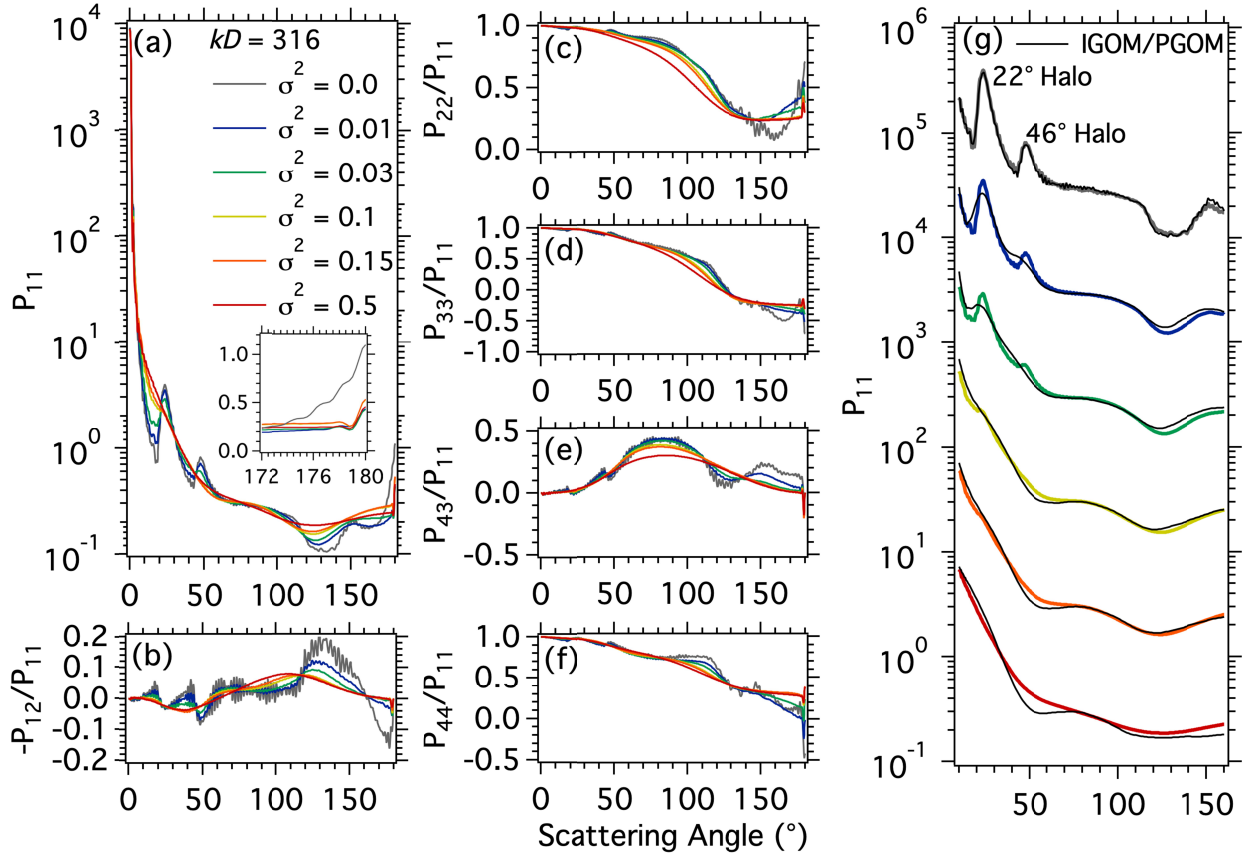
111 For larger size parameters, we use the Improved Geometric Optics Method (IGOM; Yang
112 & Liou, 1996) which is a simplified form of PGOM. However, IGOM considers the ray
113 spreading effect but the ray-tracing procedure neglects the phase interference among scattered
114 waves associated fundamentally with different outgoing rays. This simplification results in
115 inaccuracy in backscattering directions. Saito and Yang (2022b) derived a semi-physical CBE
116 correction formula from Maxwell's equations to substantially reduce the systematic biases in the
117 backscattering properties computed with IGOM. With a combination of IITM for small-to-
118 moderate size parameters ($kD \leq 316$) and IGOM with a CBE correction (hereinafter referred to
119 as IGOM+CBE) for large size parameters, the single-scattering property simulations for
120 roughened ice crystals across the entire practical size parameter range are performed. For smooth
121 particles, IITM with an efficient scheme utilizing axial symmetry is performed for $kD \leq 464$,
122 and PGOM is performed for larger size parameters.

123

124 **3 Results and Discussion**

125 3.1 Phase matrix of roughened ice crystals

126 Figure 2 shows the six nonzero phase matrix elements of compact hexagonal ice crystals
127 with various degrees of surface roughness at wavelength 532 nm, which are computed with
128 IITM. Size parameter $kD = 316$ in these simulations corresponds to an ice crystal maximum
129 diameter of 26.8 μm . Halo peaks appear at scattering angles of approximately 22° and 46° in the
130 phase functions of smooth to moderately roughened ice crystals ($\sigma^2 < 0.1$) but are suppressed
131 for more roughened ice crystals (Bi & Yang, 2014). The angular variations of the phase matrix at
132 larger scattering angles seem sensitive to smaller degrees of surface roughness. For example, the
133 phase matrices at scattering angles around halo peaks are similar between smooth and slightly
134 roughened ($\sigma^2 = 0.01$) cases, while they are different at backward scattering angles (e.g.,
135 $> 120^\circ$). Moreover, in Fig. 2a, the phase functions near the backscattering angle show distinct
136 differences between smooth and all roughened ice crystals.



137

138 **Figure 2.** (a-f) Six independent phase matrix elements (labeled on y-axis) of ice crystals with
 139 various degrees of surface roughness denoted with different colors. (g) Phase function (P_{11})
 140 curves computed with Invariant Imbedding T-matrix Method (bold lines with colors same as in
 141 panel (a)) and geometric optics methods (black lines) for the same six degrees of roughness,
 142 which are offset one order of magnitude apart.

143

144 In Fig. 2g, comparisons of the phase functions of smooth and roughened ice crystals are
 145 consistent between IITM and PGOM/IGOM across scattering angles for $\sigma^2 = 0.1-0.5$ and at
 146 backward scattering angles $90-160^\circ$ for less roughened cases. Interestingly, the halo peaks
 147 computed with IITM show similar angular widths but weaker magnitudes of their peaks as
 148 roughness increases. In comparison, the counterparts computed with IGOM tend to be broadened

149 and more rapidly suppressed when the degree of surface roughness increases, particularly for the
 150 46° halo peak (van Diedenhoven, 2014).

151 van de Hulst (1957) states that a pencil of light with its basal width of the order $l\lambda$ can
 152 retain its ray characteristics over a distance of the order $l^2\lambda$ according to the Fresnel–Huygens
 153 principle, where l and λ are the geometric width of the ray and wavelength of light. Ding et al.
 154 (2020) further validate this statement using the vector Kirchhoff integral equation. A major
 155 difference in particle geometry between smooth and roughened ice crystals is the sizes of the
 156 individual planar facets of a particle. With L defined as the maximum length of a facet of an ice
 157 crystal, we obtain $L^2\lambda \gg kD$ for a smooth ice crystal with $L = 23.19 \mu\text{m}$ but $L^2\lambda < kD$ for
 158 roughened ice crystals with $L = 0.58 \mu\text{m}$ in the present case. From the geometric optics
 159 perspective, distinct halo peaks quantified with IITM imply that the refraction of electromagnetic
 160 waves is determined mainly by the macroscopic shape rather than the small facets of the ice
 161 crystal rough surface, when the surface roughness is not significant and has a scale comparable
 162 to λ . For better understanding of these halo peaks for a roughened ice crystal from the physical
 163 perspective, the Debye series expansion of the T-matrix (Bi et al., 2018; Bi & Gouesbet, 2022)
 164 may be a useful approach.

165

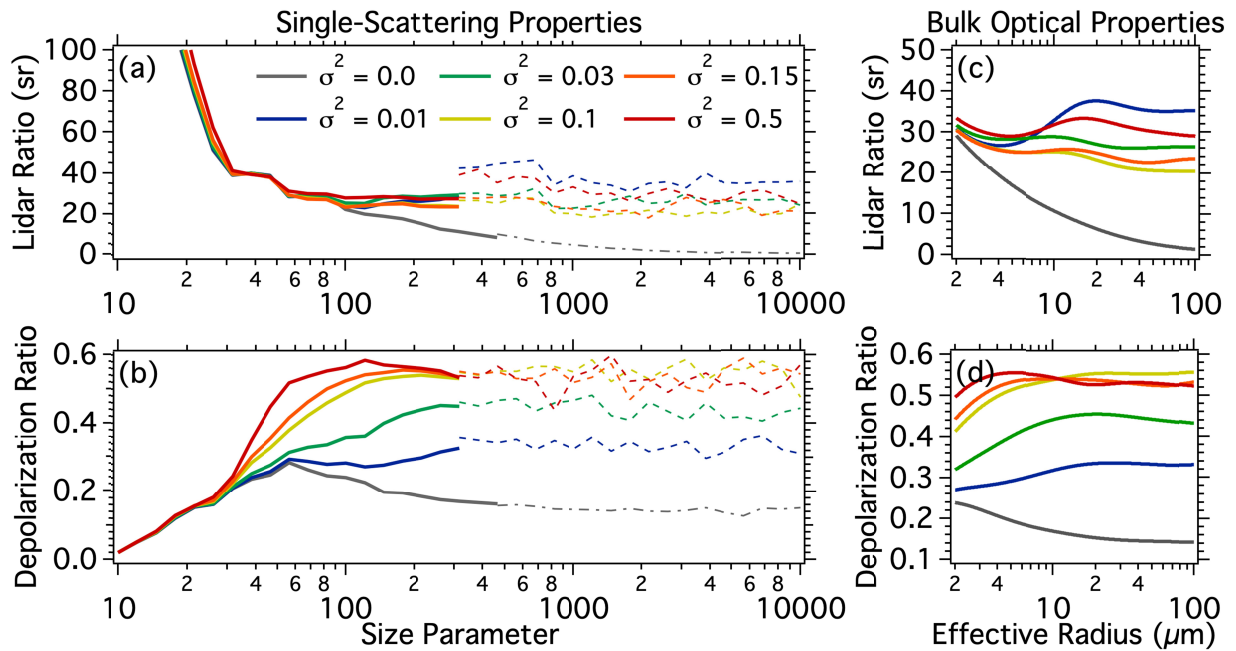
166 3.2 Lidar backscattering properties

167 The lidar ratio S and depolarization ratio δ are two fundamental backscattering properties
 168 for lidar-based remote sensing applications. For a single ice crystal, these ratios are defined as

$$169 \quad S = \frac{4\pi}{\omega P_{11}(\pi)}, \quad (2)$$

$$170 \quad \delta = \frac{P_{11}(\pi) - P_{22}(\pi)}{P_{11}(\pi) + P_{22}(\pi)}. \quad (3)$$

171 Figures 3a–b plot the lidar and depolarization ratios associated with roughened ice
 172 crystals computed with IITM and IGOM+CBE and the counterparts associated with smooth ice
 173 crystals computed with IITM and PGOM. In Fig. 3a, the lidar ratios of roughened ice crystals
 174 substantially deviate from those of smooth ice crystals with size parameters $kD > 100$. In the
 175 range of kD up to 316 simulated with IITM (corresponding to D up to 26.8 μm at wavelength
 176 532 nm), a decreasing lidar ratio with larger size parameters for smooth ice crystals originates
 177 presumably from the significant contribution of the second-order corner reflection (Borovoi et
 178 al., 2013). In Fig. 3b, the depolarization ratios exhibit pronounced sensitivities to the degree of
 179 surface roughness for size parameters $kD > 20$. The depolarization ratio levels off between 0.2
 180 for smooth and 0.55 for severely roughened ice crystals with $kD \geq 100$.



181
 182 **Figure 3.** The single-scattering (a) lidar and (b) depolarization ratios (y-axis scales), for various
 183 degrees of surface roughness (colors stated in (a)) computed with (bold solid lines) rigorous and

184 (dashed lines) geometric optics methods, for size parameters 10 to 10000 (x-axis scales). (c-d)
185 Bulk optical properties corresponding to (a-b), for effective radius 2 to 100 μm (x-axis scales).

186

187 The backscattering properties of roughened ice crystals computed with IGOM+CBE are
188 consistent with IITM at the size parameter upper limit, except with lidar ratios (Fig. 3a) for
189 $\sigma^2 = 0.01$ and 0.5 that may be associated with simplified assumptions in the CBE correction.
190 Because of weak ice absorptivity at wavelength 532 nm, the backscattering properties tend to
191 approach their respective asymptotic values for larger size parameters, as indicated by
192 IGOM+CBE simulations. In Fig. 3b, moderate fluctuations in the IGOM+CBE backscattering
193 properties originate from Monte Carlo noise associated with the ray-tracing process (Saito &
194 Yang, 2022b).

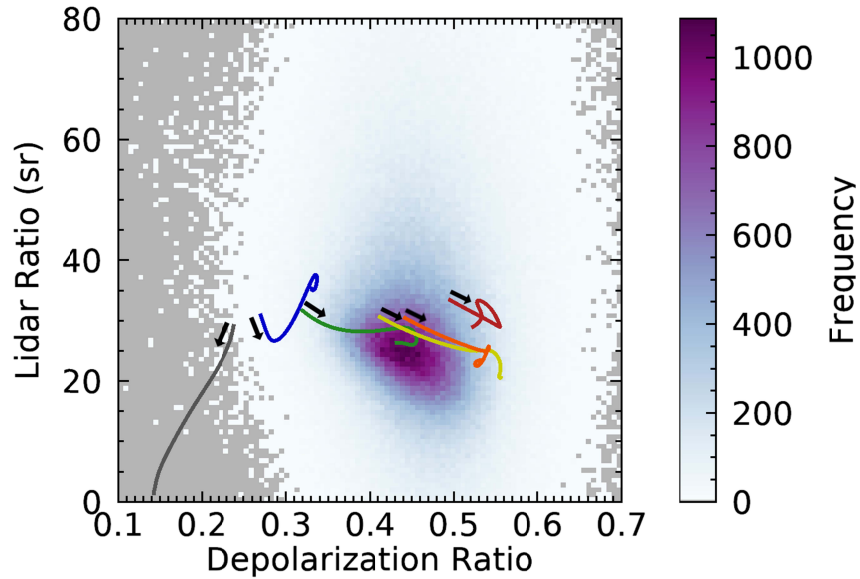
195 Bulk optical properties of polydisperse ice crystals are obtained from a weighted average
196 over the single-scattering properties of smooth and roughened ice crystals. The particle size
197 distribution (PSD) is assumed to be a gamma distribution with an effective variance of 0.26
198 (Saito & Yang, 2022a) obtained from in-situ observations of ice cloud PSDs (Heymsfield et al.,
199 2013). The bulk lidar and depolarization ratios of the polydisperse ice crystals are computed
200 based on Eqs. (1–2) with replacing the single-scattering properties with the bulk ice crystal
201 counterparts. Figures 3c–d show the bulk backscattering properties of smooth and roughened
202 hexagonal column ice crystals for effective radii 2–100 μm . The backscattering properties of
203 roughened ice crystals show a weak dependence on effective radius $> 20 \mu\text{m}$. In contrast, those
204 of a smooth ice crystal consistently show a negative correlation with effective radius.

205

206 3.3 Comparison with spaceborne lidar observations

207 We compare the theoretical backscattering properties of smooth and roughened ice
208 crystals with the counterparts estimated from the Cloud-Aerosol Lidar with Orthogonal
209 Polarization (CALIOP) observations (Winker et al., 2009). We use the version 4.20 CALIOP
210 level-2 cloud layer 5km product and select single-layer transparent cirrus clouds with a middle
211 cloud temperature $T \leq -60$ °C, where ice particles are typically small (Platt et al., 1987, 2002)
212 as less water vapor is available for ice crystal growth in a colder atmosphere. The lidar ratio is
213 derived from the constrained retrievals utilizing the two-way transmissivity of ice clouds (Young
214 & Vaughan, 2009). The particulate depolarization ratio is derived from the measured volume
215 depolarization ratio with the Rayleigh scattering contribution subtracted (Hu et al., 2009).

216 Figure 4 shows the climatological distributions of the lidar and depolarization ratios of
217 cold cirrus clouds observed by CALIOP in 2009. CALIOP points in an off-nadir direction to
218 avoid substantial influence from horizontally aligned ice crystals (Saito & Yang, 2019) in the
219 present analysis. The observed lidar and depolarization ratios are densely populated in a range S
220 of 10–45 sr and δ of 0.3–0.6. The backscattering properties of smooth ice crystals are far from
221 this range, but those of roughened ice crystals ($\sigma^2 = 0.01$ –0.5, and especially 0.03–0.15) tend to
222 be within the range. Interestingly, this roughness range is also consistent with a range of
223 estimated surface roughness from 0.01–0.3 using stereographic SEM measurements of ice
224 crystals in a laboratory (Neshyba et al., 2013, Butterfield et al., 2017).



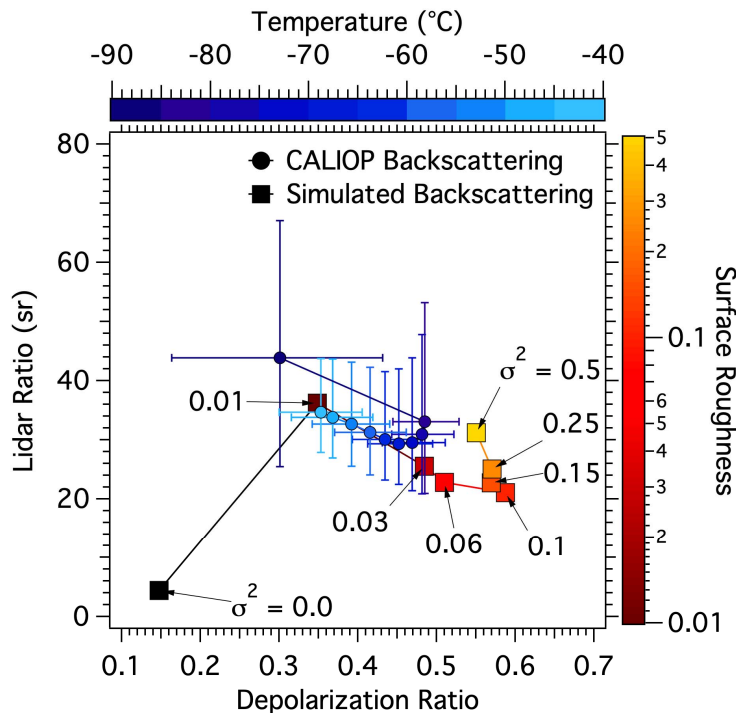
225

226 **Figure 4.** Two-dimensional histogram of the lidar and depolarization ratios of cold cirrus clouds
 227 obtained from CALIOP observations in 2009. Color lines are the theoretical counterparts along
 228 effective radii from 2–100 μm (arrows show the 2- μm starting points) with various degrees of
 229 surface roughness (same colors as in Figs. 2 and 3).

230

231 Previous studies show that smooth ice crystals with various aspect ratios exhibit limited
 232 variations of δ from 0.1–0.2 (Borovoi et al. 2013), with the exception of a smooth droxtal that
 233 shows lidar and depolarization ratios ranging from 30–40 sr and approximately 0.4, respectively
 234 (Okamoto et al., 2020). However, smooth droxtals are considered to be rare in ice clouds, as they
 235 produce specific halo peaks (Zhang et al., 2004) that are rarely observed (Sassen et al., 2003).
 236 This suggests that droxtals in ice clouds have some degree of surface roughness. Thus, we
 237 conclude that surface roughness has pronounced impacts on the backscattering properties of ice
 238 crystals and must be considered to infer the microphysical properties of ice clouds from lidar
 239 backscattering signals.

240 Reichardt et al. (2002) reported two distinct correlations among the lidar ratio,
 241 depolarization ratio, and temperature of cirrus clouds from ground-based lidar observations. A
 242 strong positive correlation between the lidar and depolarization ratios occurring at warmer
 243 temperatures (above -40°C) is well explained by the presence of horizontally oriented planar ice
 244 crystals (e.g., Saito et al., 2017). However, a reported slight negative correlation between the
 245 lidar and depolarization ratios occurring at colder temperatures (below -50°C) has been an open
 246 question. Figure 5 shows correlations among backscattering properties, temperature, and surface
 247 roughness obtained from CALIOP observations of single-layer transparent cirrus clouds with
 248 $T \leq -40^{\circ}\text{C}$ and theoretical backscattering simulations. The roughness variations can mimic the
 249 temperature dependence of the CALIOP-based backscattering properties of ice clouds. Although
 250 a definitive conclusion cannot be obtained from this analysis, a potential temperature dependence
 251 of the surface roughness of ice crystals could be a candidate to explain the slight anti-correlation
 252 of the lidar and depolarization ratios of cold cirrus clouds.



253

254 **Figure 5.** (circles) Median and quartile ranges of the lidar and depolarization ratios of ice clouds
255 with various middle cloud temperatures (indicated by blue colors) obtained from CALIOP
256 observations. (squares) Theoretical counterparts with various degrees of surface roughness
257 (indicated by red colors) and an effective radius of 30 μm are coplotted.

258

259 **4 Conclusions**

260 This study performs single-scattering property simulations of smooth and roughened
261 hexagonal column ice crystals over a wide size parameter range to investigate the impact of
262 surface roughness on backscattering properties. State-of-the-science light-scattering
263 computational methods and realistic ice crystal models reveal distinct differences in the lidar
264 ratio between smooth and roughened ice crystals. The depolarization ratio is especially sensitive
265 to the degree of surface roughness. Comparisons between theoretical backscattering properties
266 with various degrees of surface roughness and those estimated from CALIOP observations imply
267 that surface roughness is essential to robust explanation of observed lidar backscattering signals
268 associated with cold cirrus clouds, and imply possible temperature dependence of dominant
269 degrees of surface roughness of ice crystals.

270 The present study indicates a robust path forward for a better interpretation of lidar-
271 derived backscattering signals by using the microphysical properties of ice crystals. Further
272 research using sophisticated polarimetric lidar observations and these ice crystal backscattering
273 property models should provide knowledge of a wider range of morphological characteristics of
274 ice clouds.

275

276 **Acknowledgments**

277 This research was supported by NASA Grant NNH18ZD001N-RST and partly by endowment
278 funds related to the David Bullock Harris Chair in Geosciences at the College of Geosciences,
279 Texas A&M University (grant number 02-512231-0001). The numerical computations were
280 conducted with high-performance computing resources provided by Texas A&M University
281 (<https://hprc.tamu.edu>).

282

283 **Open Research**

284 The single and bulk scattering property data used in this study will be publicly available
285 (<https://doi.org/10.5281/zenodo.?????>) after the acceptance of this manuscript (the data is
286 temporarily available from Supplemental Information). CALIOP data are available through the
287 NASA Langley Research Center Atmospheric Science Data Center (<https://asdc.larc.nasa.gov/>).

288

289 **References**

- 290 Bi, L., & Gouesbet, G. (2022). Debye-series expansion of T-matrix for light scattering by
291 nonspherical particles computed from Riccati-differential equations. *Optics Express*, 30,
292 29796–29810, doi:10.1364/OE.465772.
- 293 Bi, L., & Yang, P. (2014). Accurate simulation of the optical properties of atmospheric ice
294 crystals with the invariant imbedding T-matrix method. *Journal of Quantitative*
295 *Spectroscopy and Radiative Transfer*, 138, 17–35, doi:10.1016/j.jqsrt.2014.01.013.

- 296 Bi, L., Xu, F., & Gouesbet, G. (2018). Depolarization of nearly spherical particles: The Debye
297 series approach. *Physical Review A*, 98(5), 053809.
- 298 Borovoi, A., Konoshonkin, A., and Kustova, N. (2013). Backscattering by hexagonal ice crystals
299 of cirrus clouds, *Optics Letters*, 38, 2881–2884.
- 300 Butterfield, N., Rowe, P. M., Stewart, E., Roesel, D., & Neshyba, S. (2017). Quantitative three-
301 dimensional ice roughness from scanning electron microscopy. *Journal of Geophysical*
302 *Research: Atmospheres*, 122, 3023–3041.
- 303 Cox, C., & Munk, W. (1954). Measurement of the roughness of the sea surface from
304 photographs of the sun's glitter. *Journal of the Optical Society of America* 44(11), 838-
305 850.
- 306 Cross, J. D. (1968). Study of the surface of ice with a scanning electron microscope, In *Physics*
307 *of Ice*. Munich: Plenum Press, 81–94.
- 308 Ding, J., Yang, P., Holz, R. E., Platnick, S., Meyer, K. G., Vaughan, M. A., et al. (2016). Ice
309 cloud backscatter study and comparison with CALIPSO and MODIS satellite data, *Optics*
310 *Express*, 24, 620–636, <https://doi.org/10.1364/OE.24.000620>.
- 311 Ding, J., Yang, P., Mishchenko, M. I., & Nevels, R. D. (2020). Identify the limits of geometric
312 optics ray tracing by numerically solving the vector Kirchhoff integral, *Optics*
313 *Express*, 28, 10670–10682, doi:10.1364/OE.389097.
- 314 Heymsfield, A. J., Schmitt, C., & Bansemmer, A. (2013). Ice cloud particle size distributions and
315 pressure-dependent terminal velocities from in situ observations at temperatures from 0
316 to -86°C . *Journal of the Atmospheric Sciences*, 70(12), 4123-4154.
- 317 Hioki, S., Yang, P., Baum, B. A., Platnick, S., Meyer, K. G., King, M. D., & Riedi, J. (2016).
318 Degree of ice particle surface roughness inferred from polarimetric observations,

- 319 *Atmospheric Chemistry and Physics*, 16, 7545–7558, <https://doi.org/10.5194/acp-16->
320 7545-2016.
- 321 Hu, Y., Winker, D., Vaughan, M., Lin, B., Omar, A., Trepte, C., et al. (2009).
322 CALIPSO/CALIOP cloud phase discrimination algorithm, *Journal of Atmospheric and*
323 *Oceanic Technology*, 26, 2293–2309, <https://doi.org/10.1175/2009JTECHA1280.1>.
- 324 Järvinen, E., Jourdan, O., Neubauer, D., Yao, B., Liu, C., Andreae, M. O., et al. (2018).
325 Additional global climate cooling by clouds due to ice crystal complexity, *Atmospheric*
326 *Chemistry and Physics*, 18, 15767–15781, <https://doi.org/10.5194/acp-18-15767-2018>.
- 327 Johnson B. R. (1988). Invariant imbedding T-matrix approach to electromagnetic scattering.
328 *Applied Optics*, 27, 4861–4873.
- 329 Liu, C., Panetta, R. L., & Yang, P. (2013). The effects of surface roughness on the scattering
330 properties of hexagonal columns with sizes from the Rayleigh to the geometric optics
331 regimes, *Journal of Quantitative Spectroscopy and Radiative Transfer*, 129, 169–185,
332 <https://doi.org/10.1016/j.jqsrt.2013.06.011>.
- 333 Macke, A., Mueller, J., & Raschke, E. (1996). Single scattering properties of atmospheric ice
334 crystals. *Journal of the Atmospheric Sciences*, 53(19), 2813–2825.
- 335 Magee, N., Boaggio, K., Staskiewicz, S., Lynn, A., Zhao, X., Tusay, N., et al. (2021). Captured
336 cirrus ice particles in high definition, *Atmospheric Chemistry and Physics*, 21, 7171–
337 7185, <https://doi.org/10.5194/acp-21-7171-2021>.
- 338 Magee, N. B., Miller, A., Amaral, M., & Cumiskey, A. (2014). Mesoscopic surface roughness of
339 ice crystals pervasive across a wide range of ice crystal conditions, *Atmospheric*
340 *Chemistry and Physics*, 14, 12357–12371, doi:10.5194/acp-14-12357-2014.

- 341 Neshyba, S., Lowen, B., Benning, M., Lawson, A., & Rowe, P. (2013). Roughness metrics of
342 prismatic facets of ice, *Journal of Geophysical Research: Atmospheres*, 118, 3309–3318.
- 343 Okamoto, H., Sato, K., Borovoi, A., Ishimoto, H., Masuda, K., Konoshonkin, A., & Kustova, N.
344 (2020). Wavelength dependence of ice cloud backscatter properties for spaceborne
345 polarization lidar applications. *Optics Express*, 28(20), 29178–29191.
346 <https://doi.org/10.1364/OE.400510>.
- 347 Pfalzgraff, W. C., Hulscher, R. M., & Neshyba, S. P. (2010). Scanning electron microscopy and
348 molecular dynamics of surfaces of growing and ablating hexagonal ice crystals,
349 *Atmospheric Chemistry and Physics*, 10, 2927–2935, doi:10.5194/acp-10-2927-2010.
- 350 Platt, C. M. R., Scott, S., & Dilley, A. (1987). Remote sounding of high clouds: IV. Optical
351 properties of midlatitude and tropical cirrus, *Journal of the Atmospheric Sciences*, 44,
352 729–747.
- 353 Platt, C. M. R., Young, S. A., Austin, R. T., Patterson, G. R., Mitchell, D. L., & Miller, S. D.
354 (2002). LIRAD observations of tropical cirrus clouds in MCTEX. Part I: Optical
355 properties and detection of small particles in cold cirrus, *Journal of the Atmospheric*
356 *Sciences*, 59, 3145–3162.
- 357 Reichardt, J., Reichardt, S., Behrendt, A., & McGee, T. (2002). Correlations among the optical
358 properties of cirrus-cloud particles: Implications for spaceborne remote sensing,
359 *Geophysical Research Letters*, 29, 140000–140001.
- 360 Saito M, & Yang P. (2019). Oriented ice crystals: a single-scattering property database for
361 applications to lidar and optical phenomenon simulations. *Journal of the Atmospheric*
362 *Sciences*, 76, 2635–2652.

- 363 Saito M, & Yang, P. (2022a). Generalization of atmospheric nonspherical particle size:
364 Interconversions of size distributions and optical equivalence, *Journal of the Atmospheric*
365 *Sciences*, 79, 3333–3349.
- 366 Saito, M., & Yang, P. (2022b). Critical Impacts of the Small-Scale Surface Roughness of Ice
367 Crystals on Lidar Backscattering Signals. 16th Conference on Atmospheric Radiation,
368 Madison, WI, American Meteorological Society, Session 8.2,
369 <https://ams.confex.com/ams/CMM2022/meetingapp.cgi/Paper/404577>.
- 370 Saito, M., Iwabuchi, H., Yang, P., Tang, G., King, M. D., & Sekiguchi, M. (2017). Ice particle
371 morphology and microphysical properties of cirrus clouds inferred from combined
372 CALIOP-IIR measurement, *Journal of Geophysical Research: Atmospheres*, 122, 4440–
373 4462, <https://doi.org/10.1002/2016JD026080>.
- 374 Sassen, K., Zhu, J., & Benson, S. (2003). Midlatitude cirrus cloud climatology from the Facility
375 for Atmospheric Remote Sensing, IV. Optical displays, *Applied Optics*, 42, 332–341,
376 <https://doi.org/10.1364/AO.42.000332>.
- 377 Schnaiter, M., Järvinen, E., Vochezer, P., Abdelmonem, A., Wagner, R., Jourdan, O., et al.
378 (2016). Cloud chamber experiments on the origin of ice crystal complexity in cirrus
379 clouds, *Atmospheric Chemistry and Physics*, 16, 5091–5110, [https://doi.org/10.5194/acp-](https://doi.org/10.5194/acp-16-5091-2016)
380 [16-5091-2016](https://doi.org/10.5194/acp-16-5091-2016).
- 381 Ulanowski, Z., Kaye, P. H., Hirst, E., Greenaway, R. S., Cotton, R. J., Hesse, E., & Collier, C. T.
382 (2014). Incidence of rough and irregular atmospheric ice particles from Small Ice
383 Detector 3 measurements, *Atmospheric Chemistry and Physics*, 14, 1649–1662,
384 <https://doi.org/10.5194/acp-14-1649-2014>.
- 385 van de Hulst, H. C.: *Light Scattering by Small Particles*. John Wiley and Sons, 470 pp, 1957.

- 386 van Diedenhoven, B. (2014). The prevalence of the 22° halo in cirrus clouds, *Journal of*
387 *Quantitative Spectroscopy and Radiative Transfer*, 146, 475–479.
- 388 van Diedenhoven, B., Ackerman, A. S., Fridlind, A. M., Cairns, B., & Riedi, J. (2020). Global
389 statistics of ice microphysical and optical properties at tops of optically thick ice clouds.
390 *Journal of Geophysical Research: Atmospheres*, 125, e2019JD031811.
391 <https://doi.org/10.1029/2019JD031811>.
- 392 van Diedenhoven, B., Cairns, B., Fridlind, A. M., Ackerman, A. S., & Garrett, T. J. (2013).
393 Remote sensing of ice crystal asymmetry parameter using multi-directional polarization
394 measurements – Part 2: Application to the Research Scanning Polarimeter, *Atmospheric*
395 *Chemistry and Physics*, 13, 3185–3203, <https://doi.org/10.5194/acp-13-3185-2013>.
- 396 Winker, D. M., Vaughan, M. A. Omar, A. Hu, Y. Powell, K. A. Liu, Z. et al. (2009). Overview
397 of the CALIPSO mission and CALIOP data processing algorithms, *Journal of*
398 *Atmospheric and Oceanic Technology*, 26, 2310–2323.
- 399 Yang, P., & Liou, K. N. (1996). Geometric-optics-integral-equation method for light scattering
400 by nonspherical ice crystals, *Applied Optics*, 35, 6568–6584.
- 401 Yang, P., & Liou, K. N. (1997). Light scattering by hexagonal ice crystals: Solution by a ray-by-
402 ray integration algorithm, *Journal of the Optical Society of America A.*, 14, 2278-2289.
- 403 Yang, P. & Liou, K. N. (1998). Single-scattering properties of complex ice crystals in terrestrial
404 atmosphere, *Contributions to Atmospheric Physics*, 71 (2), 223–248.
- 405 Yang, P., Ding, J., Panetta, R. L., Liou, K.-N., Kattawar, G. W., & Mishchenko, M. I. (2019). On
406 the convergence of numerical computations for both exact and approximate solutions for
407 electromagnetic scattering by nonspherical dielectric particles, *Progress in*
408 *Electromagnetic Research*, 164, 27–61.

- 409 Yang, P., Hong, G., Kattawar, G. W., Minnis, P., & Yongxiang, H. (2008). Uncertainties
410 associated with the surface texture of ice particles in satellite-based retrieval of cirrus
411 clouds: Part II; Effect of particle surface roughness on retrieved cloud optical thickness
412 and effective particle size, *IEEE Transactions on Geosciences and Remote Sensing* 46,
413 1948–1957.
- 414 Yi, B., Yang, P., Baum, B. A., L’Ecuyer, T., Oreopoulos, L., Mlawer, E. et al. (2013). Influence
415 of ice particle surface roughening on the global cloud radiative effect, *Journal of the*
416 *Atmospheric Sciences*, 70, 2794–2807.
- 417 Young, S. A. & Vaughan, M. A. (2009). The retrieval of profiles of particulate extinction from
418 Cloud Aerosol Lidar Infrared Pathfinder Satellite Observations (CALIPSO) data:
419 Algorithm description, *Journal of Atmospheric and Oceanic Technology*, 26, 1105–1119,
420 <https://doi.org/10.1175/2008JTECHA1221.1>.
- 421 Zhang, Z., Yang, P., Kattawar, G. W., Tsay, S.-C., Baum, B. A., Huang, et al. (2004), Geometric
422 optics solution to light scattering by droxtal ice crystals, *Applied Optics*, 43, 2490–2499,
423 doi:10.1364/AO.43.002490.
- 424 Zhou, C. & Yang, P. (2015). Backscattering peak of ice cloud particles, *Optics Express*, 23,
425 11995–12003.